Broadband inverted T-shaped seismic metamaterial

Yi Zeng, Shu-Yan Zhang, Hong-Tao Zhou, Yan-Feng Wang, Liyun Cao, Yifan Zhu, Qiu-Jiao Du, B. Assouar, Yue-Sheng Wang

Broadband inverted T-shaped seismic metamaterial

Yi Zeng[1, 2], Shu-Yan Zhang[3], Hong-Tao Zhou[1], Yan-Feng Wang[1], Liyun Cao[2], Yifan Zhu[2], Qiu-Jiao Du[4], Badreddine Assouar[2, *] and Yue-Sheng Wang[1, *]

[1]*Department of Mechanics, School of Mechanical Engineering, Tianjin University, Tianjin 300350, China*

[2] *Institut Jean Lamour, CNRS, University de Lorraine, Nancy 54506, France*

[3] *Institute of Engineering Mechanics, Beijing Jiaotong University, Beijing 100044, China*

[4] *School of Mathematics and Physics, China University of Geosciences, Wuhan 430074, China*

* Electronic mail: badreddine.assouar@univ-lorraine.fr (B. Assouar), yswang@tju.edu.cn (Y.-S. Wang).

Abstract

Seismic metamaterials (SMs) are expected to assist or replace traditional isolation systems owing to their strong attenuation of seismic waves. In this work, a one-dimensional inverted T-shaped SM (1D ITSM) composed of arrays of inverted T-shaped structures on a half space is proposed, which have an ultra-wide first bandgap (FBG) from 6.7 to 17.2 Hz. We find that the FBG is composed of two parts; part 1 with surface evanescent waves from 6.7 to 11.0 Hz and part 2 with no surface modes from 11.0 to 17.2 Hz by using the complex band structures. The propagation of seismic surface waves in the 1D ITSM is different in these two frequency ranges of the FBG. In part 1, the seismic surface waves are significantly attenuated in the 1D ITSM because of the surface evanescent waves, while in part 2, the surface waves are converted into bulk waves because surface waves cannot exist in the ITSM. Finally, the ultra-wide FBG is verified by using a kind of the two-dimensional ITSM in large-scale field experiments.

Kay words: seismic metamaterials, surface waves, inverted T-shaped, first bandgap, relative bandwidth, large-scale field experiments

Introduction

Metamaterials[1-6] are a kind of composite material composed of periodically arranged artificial unit cells. One of the most significant characteristics of metamaterials is the bandgap (BG).[7-11] In the frequency range of the BG, waves cannot propagate in the metamaterials. This characteristic is used by physicists to control the propagation of seismic waves, thereby preventing casualties and property damage caused by the destruction of buildings. This kind of metamaterial used to control seismic waves is called seismic metamaterial (SM).[12-16] The SM can be used to protect critical infrastructures and most buildings located in the mid- and far-fields of the earthquake source. It is worth noting that the natural frequency of these buildings is below 20 Hz.[12, 17] Therefore, the realization of the SM with ultra-low BGs is an important step to push the SM to practical application. The conjecture of the SM was proposed after the experiment of the phononic crystal in marble in 1999.[7] The attenuation of the elastic surface waves in the two-dimensional crystals identified the existence of the bandgaps. However, a large amount of research on the SMs began in 2014. In this year, cylindrical holes arranged periodically in soil were experimentally proved to attenuate seismic waves at 50 Hz.[14] Previous works have demonstrated the propagation of seismic waves generated by the probe in the phononic crystals. Results show that it was consistent with the numerical simulation based on the approximate plate model. These large-scale experiments on the SM have shown that it has unlimited potential in controlling seismic waves. Later, researchers changed the shape of the holes, and filled different materials into the holes to obtain the SMs with a wide BG.[18-20] However, the structure of this kind of SM based on the Bragg scattering mechanism is very huge to control ultra-low-frequencies seismic waves, which makes it difficult for practical application. Fortunately, the SMs based on local resonance can solve this problem, which can use small structures to control long waves.[21-24] Therefore, most of these SMs are also called subwavelength

SMs.[25-27] The subwavelength SMs can be roughly divided into two categories. The first kind of subwavelength SMs can also be called the underground barrier of locally resonant metamaterial.[15, 28-31] This kind of underground SMs with small scale is based on resonance characteristics to attenuate long-wavelength seismic waves.[21] However, their BGs are generally narrow. On the other hand, these resonant unit cells should be placed where the elastic waves propagate to better attenuate the seismic waves. For example, the depth of these SMs burial into the ground should be roughly equal to twice the wavelength of the seismic surface wave to better attenuate them[32]. In this way, although the dimensions of every unit cells are very small, the depth of burial is isolating. The second kind of subwavelength SMs are usually composed of periodic pillar-like structure and substrate, which can be called the pillar-like SM (PSM). A major characteristic of the PSM is that it mainly attenuates the propagation of seismic surface waves,[33, 34] especially in the low-frequency range of the first BG (FBG), and even if the PSM only has three rows.[34, 35] The PSM is found because seismic surface waves in a part of the frequency range cannot pass through forest.[34] When the seismic waves interact with a forest, some frequencies are strongly attenuated due to the resonance of trees. When trees are considered as steel pillars or pillars with different shapes, the attenuation of surface waves in the SMs still exists, and better results can be obtained. So, I-shaped,[35] fractal structure [36] and Matrayoshka-like [37] PSMs are proposed to obtain a wider complete BG in the sound cone. However, the relative bandwidth of the FBG is currently too small to meet the needs of practical applications.

In this paper, a one-dimensional inverted T-shaped SM (1D ITSM) composed of pillars and plates with ultra-wide FBG is proposed. The ITSM is just a simple modification based on the PSM: a plate is added at the bottom of each pillar. The FBGs of the two different SMs are compared. The effects

of the ITSM's geometric and material parameters on the FBG are discussed. The complex band structure of the ITSM for surface waves is calculated and compared with that of the PSM. The propagation properties of seismic surface waves in the ITSM are also given. Finally, we propose a kind of the two-dimensional (2D) ITSM with the ultra-wide FBG.

1. Model of the 1D ITSM

In this section, the classical PSM and the proposed 1D ITSM are compared. As shown in Fig. 1, the PSM and the ITSM have the same steel pillar, i.e., $l_2 = l$, $w_2 = w$. But the bottom of every pillar in the ITSM is clamped by a steel plate marked as gray part in Fig. 1(b). The geometric and material parameters of the unit cells are given in Tables 1 and 2, respectively. In numerical simulation, the left and right boundaries of the substrate of the unit cell are set as Bloch periodic boundaries, and the bottom of the substrate is set as a fixed boundary condition to avoid surface modes on the bottom.[19, 20, 37] It is worth noting that the calculation results will converge well at ultra-low frequency when the geometric parameter H is enough large. In this paper, the COMSOL Multiphysics is used to calculate the band structures and the propagation of Rayleigh waves in the SMs.

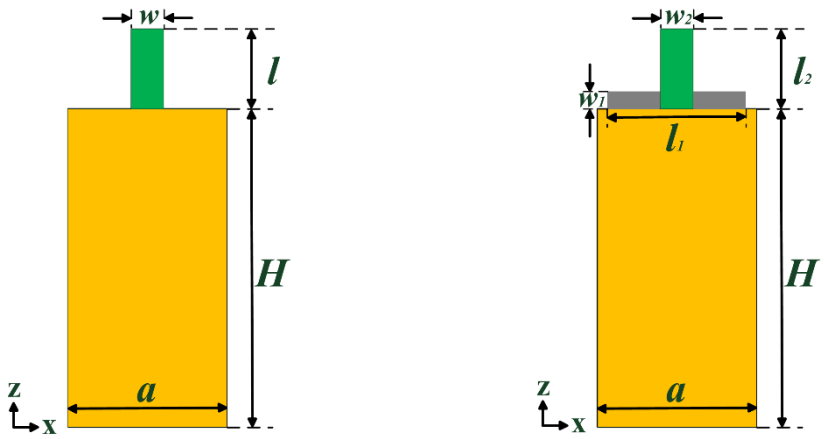

(a) (b)

Figure 1: The unit cells of (a) the PSM and (b) the 1D ITSM.

a	H	l_1	w_1	$l_2(l)$	$w_2(w)$
1.5 m	300 a	0.95 a	0.05 a	1.4285 a	0.07 a

Table 1: The geometric parameter of the PSM and the 1D ITSM

Material	Density (kg/m^3)	Young's modulus (Pa)	Poisson's ratio
Steel	7784	2.07×10^{11}	0.3
Soil	1800	2×10^{7}	0.3

Table 2: The material parameters used in this paper[18, 28, 30]

2. Results and Discussion of the 1D ITSM

2.1 Classical band structure

Figures 2 (a - b) show the classical band structures of the PSM and the ITSM, respectively. The classical band structures are calculated by using the Solid Mechanics module of COMSOL. The sound cones are clearly surrounded by the light gray areas. There are only surface waves inside the sound cone. Therefore, surface waves cannot exist in the SMs in the frequency range where no band appears, i.e., the bandgap for surface waves. Moreover, the bandgaps at the lowest frequency, i.e., the FBGs, are marked by the dark gray areas in Figs. 2 (a - b). In this work, the frequency range of the FBG is from 0.72 Hz to 0.80 Hz for the PSM, and from 6.7 Hz to 17.2 Hz for the ITSM. Although the FBG of the PSM is very low, it is extremely narrow (relative bandwidth is about 0.1) and thus unsuitable for seismic shielding. In contrast, although the minimum value of the FBG of the ITSM is 6.7 Hz, its relative bandwidth can reach an astonishing value as 0.88. We believe that this way of abandoning the BG with ultra-low frequency in exchange for the ultra-wide BG is desirable in the practical application of SMs.

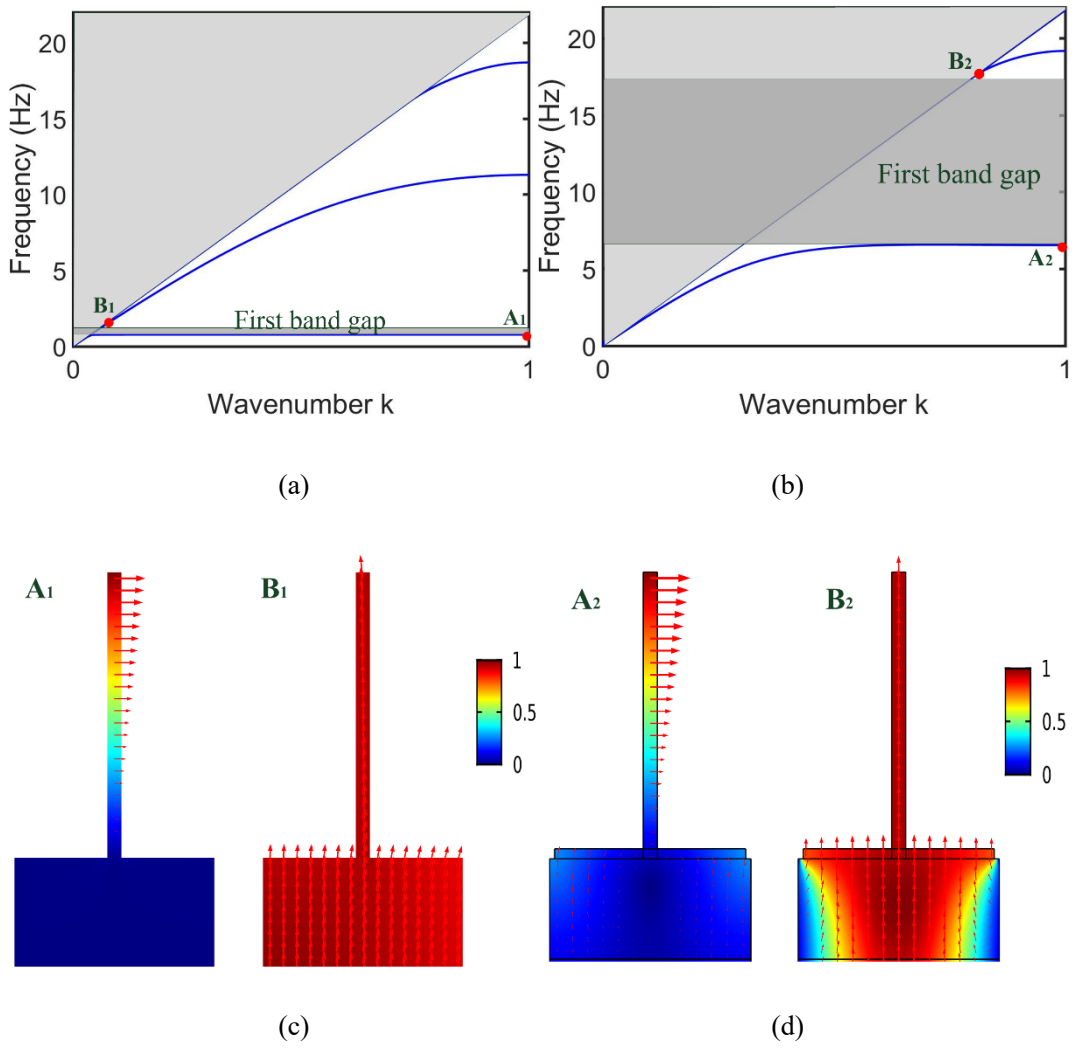

Figure 2: The classical band structure of (a) the PSM and (b) the 1D ITSM, the vibration modes of (c) the PSM and (d) the 1D ITSM at the points marked the classical band structures.

The vibration modes of the PSM and the ITSM at marked points are illustrated in Figs. 2 (c - d). The marked points A_1 and B_1 (A_2 and B_2) are the lower and upper boundaries of the FBG of the PSM (ITSM), respectively. The direction of the arrows represents the direction of the particle movement, and the color indicates the normalized total displacement. It is easy to find that the vibration modes of the lower, upper boundaries of the two FBGs (points A_1 and A_2, points B_1 and B_2) are similar. This indicates that the generation mechanism of these two FBGs is also similar. On the first bands of two SMs, i.e., at points A_1 and A_2, the maximum displacement appears on the top

of the steel structure. On the second bands of two SMs, i.e., at points B_1 and B_2, the displacement is on the entire steel structure and on the surface of substrate. The energy is evenly distributed on the entire structure. The pillar or the inverted T-shaped structure (ITS) can be considered as a whole this time. This shows that the structure of the ITS leads to a qualitative leap of the FBG. It is worth noting that although the second bandgap in Fig. 2(a) is similar to the FBG in Fig. 2(b), these two bandgaps have different generation physical mechanisms, which have been identified by many experiments and numerical simulations.[24, 35, 37]

2.2 Effects of geometric parameters

After comparing the band structures of the PSM and the ITSM, it is obvious that the appearance of the plate at the bottom of the pillar makes a huge change in the frequency range and relative bandwidth of the FBG. In this section, the effects of geometric parameters of the plate on the FBG are calculated, when the pillar is unchanged. In addition, the effect of the height of the pillar on the FBG is calculated to obtain the optimal geometric parameters of the ITSM, when the total volume of the pillar (i.e., $l_2 \times w_2$) is constant.

Figures 3(a - b) show that the variation of geometric parameters of the plate with the position and relative bandwidth of the FBG. As shown in Fig. 3(a), when the length l_1 of the plate increases from 0.5a to 0.99a, the lower boundary of the FBG slowly increases from 4.4 Hz to 7.0 Hz, and the upper boundary increases rapidly from 5.7 Hz to 20.7 Hz. Therefore, the relative bandwidth of the FBG increases from 0.27 to 0.99. As shown in Fig. 3(b), when the width of the plate increases from 0.02a to 0.18a, the lower boundary of the FBG first grows slowly from 5.5 Hz to 6.7 Hz, and then slowly drops to 6.4 Hz. However, the upper boundary of the FBG increases rapidly from 9.0 Hz to 17.2 Hz, and then slowly decreases to 13.7 Hz. Therefore, the relative bandwidth of the FBG increases rapidly

from 0.47 to 0.88, and then slowly drops to 0.73.

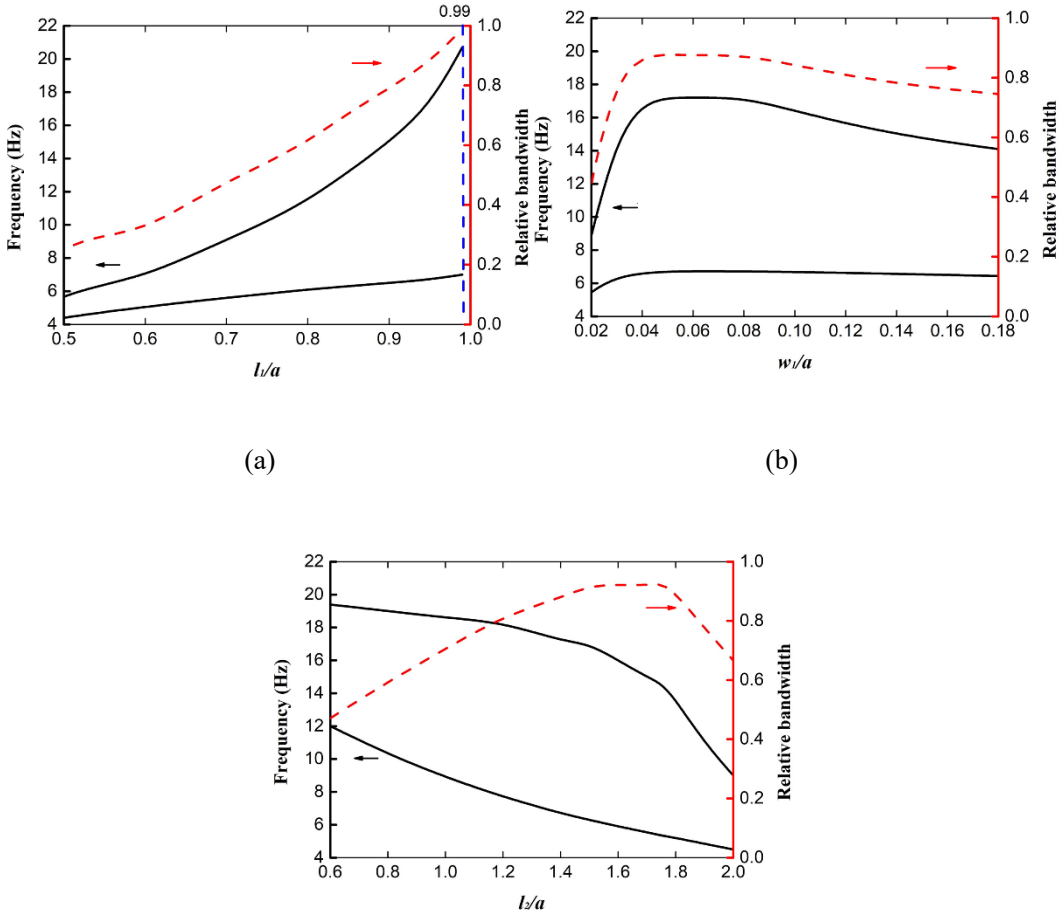

Figure 3: Variation of the upper and lower frequency boundaries, and the relative bandwidth of the FBG with the ratio of the geometric parameters (a) l_1, (b) w_1 and (c) l_2 to lattice constant a. The black solid line is the upper and lower boundaries of the FBG, and the red dashed line is the relative bandwidth.

Figure 3(c) shows the effect of the pillar height on the FBG. When the pillar height continues to increase from 0.6a to 1.7a, the upper and lower boundaries of the FBG continue to decline, and its relative bandwidth continues to increase. But when the pillar height is greater than 1.8a, the upper boundary of the FBG drops rapidly, leading to the decrease of the relative bandwidth. Therefore, when the pillar height is about 1.7a, the relative bandwidth of the FBG of the ITSM is the largest,

about 0.93.

The results show that the geometric parameters of the plate and pillar in the ITS have an obvious effect on the relative bandwidth of the FBG. With the appearance of the plate and the increase in its length, although the center frequency of the FBG of the ITSM continues to increase, its relative bandwidth increases linearly. However, there is an optimal value for the thickness of the steel plate, about 0.05a. When the height of the pillar continues to increase within a certain range, the center frequency of the FBG continues to decrease, but the relative bandwidth continues to increase. However, when the pillar is too high and its width is too small ($l_2 \times w_2$ is constant), the decrease in the flexural resonance frequency of the pillar causes the relative bandwidth to decrease continuously.

2.3 Effects of material parameters

In this section, the influence of material parameters of the ITS on the FBG is analyzed. Material parameters of the ITS are swept only for qualitative comparison.[38] Only one parameter is changed at a time, and other parameters are consistent with those in Fig. 1(b).

The effect of mass density of the ITS (ρ_{ITS}) on the FBG is shown in Fig. 4(a). When ρ_{ITS} increases from 4000 kg/m^3 to 10000 kg/m^3, the lower boundary of the FBG decreases from 9.1 Hz to 6.0 Hz; and the upper boundary reduces from 21.0 Hz to 14.5 Hz. The center frequency of the FBG keeps dropping. However, the relative bandwidth first increases and then decreases, and its maximum value is about 0.9 when ρ_{ITS} is about 7000 kg/m^3. The effect of Young's modulus of the ITS (E_{ITS}) on the FBG is shown in Fig. 4(b). When E_{ITS} increases from 50 GPa to 350 GPa, the lower boundary increases slightly. When E_{ITS} increases from 50 GPa to 180 GPa, the upper boundary rapidly increases from 10.0 Hz to 17.0 Hz. Finally, the frequency slowly increases to 18.2 Hz, when E_{ITS} increases from 180 GPa to 350 GPa. Therefore, the relative bandwidth rapidly increases from 0.54

to 0.88, and it has just little change when E_{ITS} is larger than 180 GPa. These results show the ITSM has the FBG with largest relative bandwidth when ρ_{ITS} is about 7000 kg/m^3 and E_{ITS} is larger than 180 GPa. In reality, steel is the best choice for the ITS.

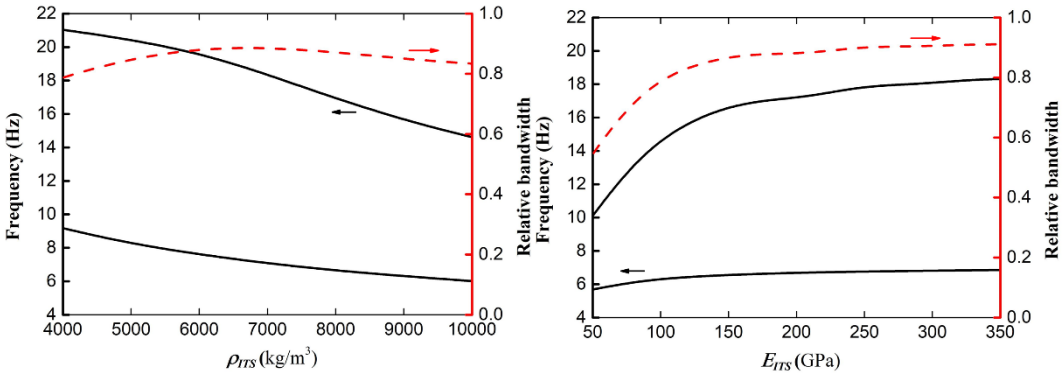

(a) (b)

Figure 4: Variation of the upper and lower frequency boundaries, and the relative bandwidth of the FBG (a) the mass density ρ_{ITS} and (b) the Young's modulus E_{ITS}. The black solid line is the upper and lower boundaries of the FBG, and the red dashed line is the relative bandwidth.

2.4 Complex band structure

In order to deeply explore the wide FBG of the ITSM, the complex band structures shown in Fig. 5(a), are calculated by using the PDE module of the COMSOL. The complex band structures of seismic metamaterials are considered when the wave vector is complex. The negative wave vector means that the amplitude of elastic wave is attenuated in the space, i.e., there is a surface evanescent wave.[38, 39] In order to draw only the surface modes in the complex band structure, the following parameter ξ is introduced,[19, 32]

$$\xi = \int_{S(2\lambda)} |\boldsymbol{u}| ds \,/\, \int_{S(H)} |\boldsymbol{u}| ds \ , \tag{1}$$

that is, in the displacement fields of the ITSM, the ratio of the integral of the displacement ($\boldsymbol{u}$) in the range of depth of twice the Rayleigh wave wavelength (2λ) below the surface to the integral of the

displacement over the entire depth (H) of the substrate. The parameter ξ can be used to filter all surface modes from the complex band structure by using the displacement fields calculated with the finite element method (COMSOL Multiphysics). In this paper, the surface mode is defined as $\xi > 0.9$. This is because when the parameter $\xi > 0.9$ in one mode, i.e., more than 90% of the energy in a unit cell all exists near the surface, this mode can be deemed as a surface mode. In Fig. 5(a), the color bar on the far right represents the value of ξ. The black dotted line is the boundary of the sound cone.

In the complex band structure of the ITSM, the FBG can be divided into two completely different parts: part 1 with surface evanescent waves (light gray); part 2 with no surface mode (heavy gray). From the real part of the complex band structure of the ITSM, there is a surface band in the FBG in part 1, with a frequency range from 6.7 Hz to 11.0 Hz. This band partially overlaps with the first band at about 6.7 Hz. In the imaginary part of the surface band in part 1 are all greater than zero. They are surface evanescent waves in this frequency range and cannot be displayed in the classical band structure. The vibration mode at the end of the band is plotted. It can be found that most of the vibration exists in the substrate and decreases with increasing depth. We speculate that as the frequency increases, most of the vibration is transferred to the substrate thus the surface mode disappears. In part 2 with the frequency range of 11.0 Hz to 17.2 Hz, there is no surface band in the complex band structure of ITSM. Similar phenomenon is currently only found in the inverse dispersion SMs (Notes A and B in Supplementary Information (SI)). We speculate that in this frequency range, the steel structure can be equivalent to a layer of uniform medium on the substrate due to its longitudinal resonance (vibration perpendicular to the surface of the substrate). The layered media structure composed of this medium and the substrate has an inverse dispersion BG.

In this frequency range of the BG, the surface waves will be converted into bulk waves (Note B of SI).

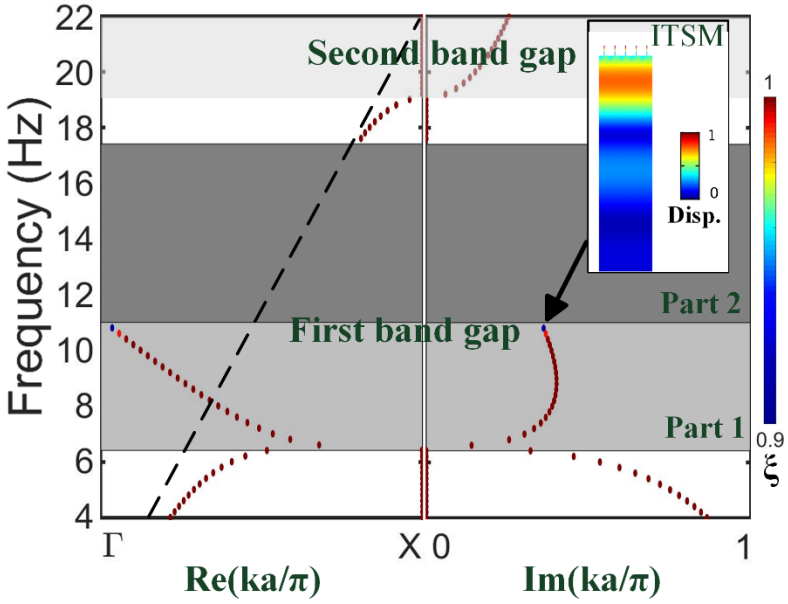

(a)

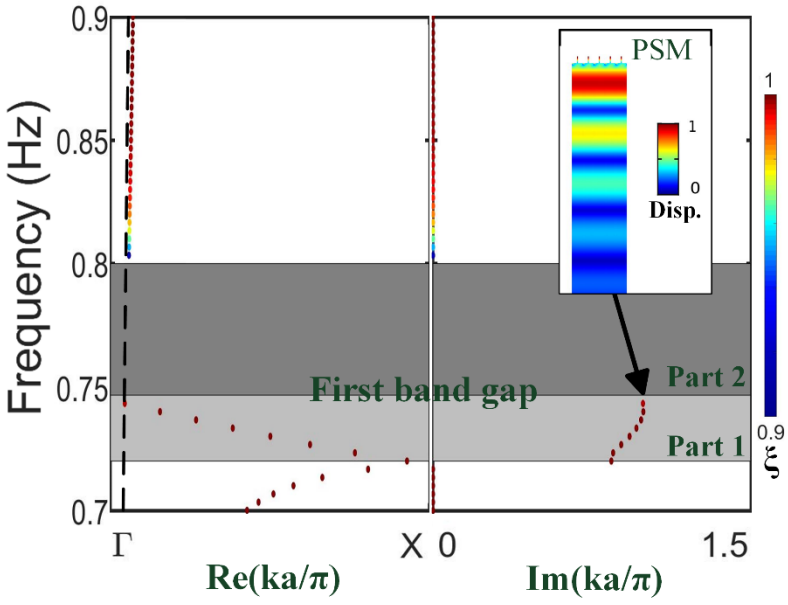

(b)

Figure 5: The complex band structures of (a) the 1D ITSM and (b) the PSM. The first bandgap composes of two parts: 1 and 2. There are evanescent surface waves in the part 1 and no surface mode in part 2. The color bars from 0.9 to 1 on the far right represent the value of ξ. The inset contents show the vibration modes at the end of the bands

in parts 1. The color bars from 0 to 1 represent the displacement in the vibrating modes.

Similarly, as shown in Fig. 5(b), as a comparison, the complex band structure of the FBG of the PSM shown in Fig. 1(a) is calculated. It is easy to find that the situation in these two FBGs is almost identical. So, we believe that the formation mechanism of these two FBGs is almost the same.

2.5 Frequency domain analysis

The transmission spectrum is calculated in this section. The finite model used for calculation is shown in Fig. 6(a), and consisting of two parts: the substrate represented by the yellow part, and the periodic ITSs represented by the gray part and the green part. The material and geometric parameters of the ITS are consistent with those in Fig. 1(b). The boundaries of the left, right, and bottom of the substrate are set as low reflection boundary condition to eliminate the reflection of elastic waves.[19, 20] The number of rows of the ITSM is 10. Point A is set as the source to generate Rayleigh waves. The polarization direction of the source is the *xz* direction.[26, 40, 41] Accordingly, the data is collected at point B from the right side of the ITSM. Similarly, in order to obtain an accurate transmission spectrum at a sufficiently low-frequency range, the height of the substrate is set as $H = 300a$. The acceleration at point B is collected with and without the ITSM. When there is the ITSM, the acceleration at point B is A_1. When there is no ITSM, the acceleration at point B is A_0. The transmission is defined as $T = 20 \times \log_{10}(A_1 / A_0)$.

As shown in Fig. 6(b), the ITSM has a very significant attenuation effect on the Rayleigh waves in the frequency range of the FBG. There is a huge attenuation zone from 6.7 Hz to 17.2 Hz, consistent with the range of the FBG in Fig. 2(b). This result shows that the ITSM can drastically attenuate the Rayleigh waves at a sufficiently low frequency and in a wide range. In addition, it is easy to find that in the FBG's two different parts identified in complex band structure (Fig. 5(a)), the attenuation

effects of the ITSM on Rayleigh waves are completely different. Because there are evanescent surface waves in part 1, the attenuation effect in part 1 is more pronounced than that in part 2. In part 1, the larger the value of the imaginary part is, the stronger the attenuation effect of the ITSM on Rayleigh waves is. Moreover, there is a strong attenuation of the surface waves from 19.1 to 22.0 Hz shown in Fig. 6(b). This is because that, in the second bandgap of the ITSM, there are evanescent waves shown in Fig. 5(a), and the surface waves are converted into bulk waves [37].

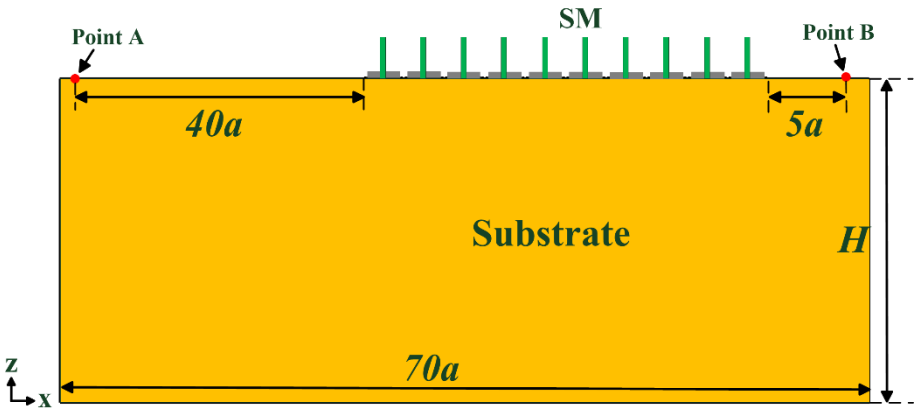

(a)

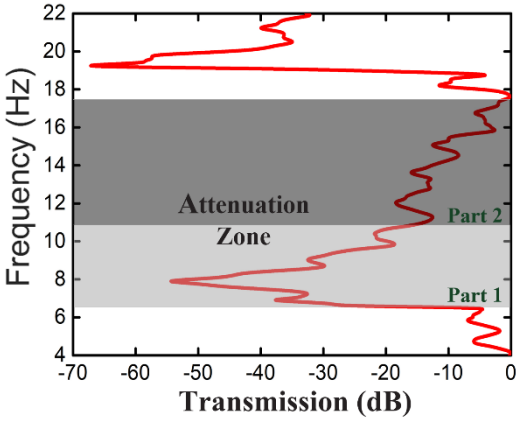

(b)

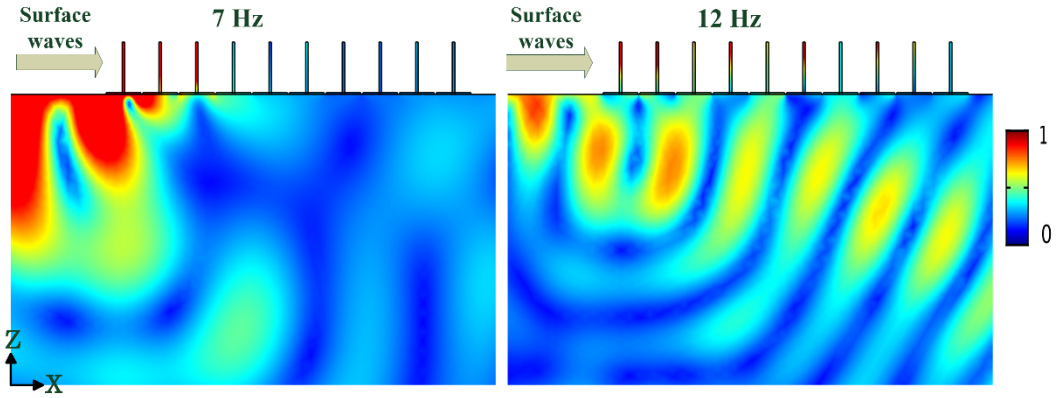

(c)

Figure 6: (a) Schematic model of the 1D ITSM with 10 unit cells for transmission calculations. (b) Transmission spectrum of the ITSM at the frequency range from 4 Hz to 22 Hz. (c) Distribution of displacement amplitude in the ITSM at 7 Hz and 12 Hz.

As shown in Fig. 6(c), the distribution of displacement amplitude in the ITSM is given at two different but representative frequencies in the FBG: 7.0 Hz and 12.0 Hz. In the frequency range of part 1, for example, at 7.0 Hz, the violent resonance of the ITSM causes the surface waves to be significantly attenuated and almost unable to propagate to the third unit cell. In the frequency range of part 2, for example, at 12.0 Hz, after the surface waves enter the ITSM, we can observe that the surface waves are converted into bulk waves. These two results are easily reminiscent of the literature, [33] where surface waves are incident from two ends of the metawedge. When the surface wave is incident from the short edge, the surface waves first encounter part 1 of the FBG of the shorter PSM. So, the surface wave is quickly attenuated because of the evanescent waves. When the surface wave is incident from the taller end, the surface waves first encounter part 2 of the FBG of the taller PSM. So, the surface waves are converted into bulk waves because of the inverse-dispersion effect (Note A in SI). This also indirectly proves that the formation mechanism of the FBG of the PSM and the ITSM is almost the same. So, in this work, the bandgap from 6.7 to 11 Hz

is used to stop the propagation of the Rayleigh waves. And the bandgap from 11 to 17.2 Hz is used to convert Rayleigh waves into bulk waves. In conclusion, the ultra-wide bandgap from 6.7 to 17.2 Hz is useful to attenuate Rayleigh waves to protect the aimed buildings. Moreover, the propagation of the Rayleigh waves is studied when the bottoms of the steel structures are buried in the substrate. The result is shown in Note C of SI.

3. The 2D ITSM and large-scale field experiments

For the SM, a 1D periodic model is a general choice for exploring mechanism of the BGs.[20, 26, 32] This is because it is a common method to study the SMs for surface waves, especially for Rayleigh waves, whose displacement components on the surface only exist in the *x* and *z* directions [40]. These two directions are both considered in the 1D simulations. Therefore, the 1D simulation is the basic study of the elastic metamaterials for surface waves. We can easily investigate the bandgap characteristic and the mechanism of bandgaps to easily design the 2D elastic metamaterials. However, in practical applications, the design of the 2D periodic SM is more important and necessary.[18, 37, 42] In addition, due to some uncontrollable factors in actual situations, such as the difficulty of achieving perfect continuity between different materials, large-scale field experiments are still needed to verify the SMs with ultra-wide and low-frequency bandgaps for surface waves. Therefore, based on the design concept and the mechanism of the above-mentioned 1D ITSM, a kind of 2D ITSM and a large-scale field experiments are designed for isolating Rayleigh waves in this section. It is worth noting that due to the experimental equipment and test site, the 2D ITSM with smaller dimensions than the 1D ITSM are chosen. However, the operating frequency and frequency range of the 2D ITSM are lower and much wider than the SMs that has been experimentally verified.[14, 34]

3.1 Designs of the 2D ITSM and experimental setup

Fig. 7(a) shows the unit cell of the 2D ITSM designed according to the structure of the 1D ITSM. In order to facilitate field experiments and attenuate seismic surface waves in the lower frequency range, the lattice constant a_1 of the unit cell is set as 0.25m. And the unit cell is composed of a thumbtack-shaped structure (purple part) and a soil substrate (gray part). Among them, the thumbtack-shaped structure (TS) is composed of a steel tube and a steel plate. The geometric parameters of the unit cell are shown in Table 3. As shown in Fig. 7(b), the central garden of the Department of Mechanics on the Beiyangyuan Campus of Tianjin University (China) was selected for a large-scale field experiments in August 2020. The geometric parameters of the TS used in large-scale filed experiments are consistent with those in Fig. 7(a). Among them, the steel tube and steel plate are rigidly connected by high-strength bolts. 25 identical TSs are customized and periodically arranged on the substrate.

a_1	b	t	h	D	d
0.25 m	0.2375 m	0.012 m	0.75 m	0.051 m	0.041 m

Table 3: The geometric parameters of the unit cell in Fig. 7(a)

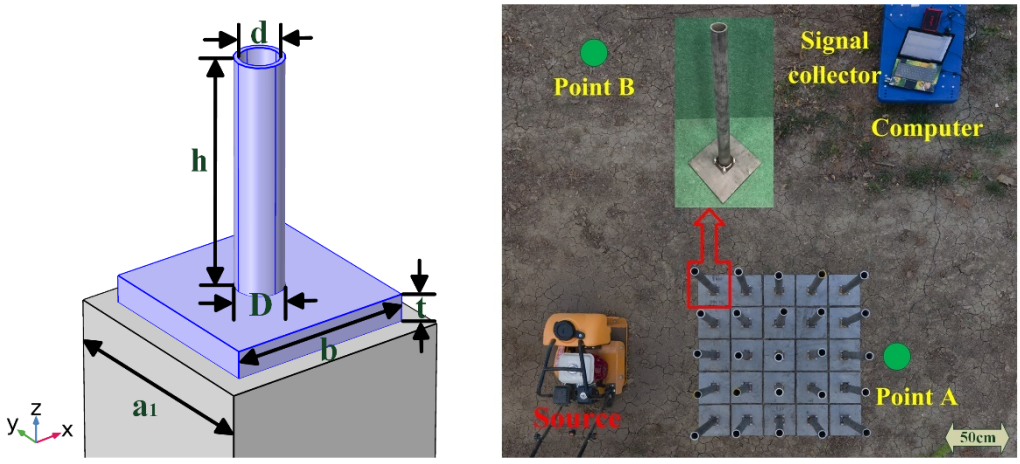

(a) (b)

Figure 7: (a) Schematic of the unit cell and (b) top view of the experimental setup. Points A and B are signal acquisition points, and point B is the reference point.

Considering the viscoelasticity and non-uniformity of the soil, we use the controlled variable method: using two sensors (uT, A21D100) with the same distance to the source to measure the acceleration of the two points (points A and B shown in Fig. 7(b)). The vibration source is generated by the rammer (Mingtu Mechanics, C90t) with an exciting force of 20kN. The data of two sensors is collected by the signal collector (uT, uT3604FS-ICP), and processed by the computer to obtain the response results at the two points. When the TSs are not placed in the field, the responses of the two points are almost the same when the rammer works. Therefore, this experiment can almost eliminate most uncontrollable factors, and only focus on the influence of the presence of artificial structures on the propagation of Rayleigh waves. The transmission of Rayleigh waves by the TSM is defined as $20*\log_{10}(A_A/A_B)$ [20], where A_A and A_B are the accelerations in the vertical direction of points A and B, respectively. The material parameters of the tests is referenced in these literatures [28, 30], which is same as in Tables 2. It is worth noting that in the tests, the TS is simply placed on the substrate. But in the simulation mentioned above, the TSs and soil are perfectly continuous.

3.2 Results of the 2D ITSM and field experiments

The band structure of the 2D ITSM only in the ΓX direction is calculated to facilitate comparison with the experiments, as shown in Fig. 8(a).[18, 37, 43] The sound cone is clearly surrounded by the light gray areas. The whole band structure along Γ-X-M-Γ direction in the first Brillouin zone can be found in the Note D of SI. The vibrating mode of the highest point of the first band is given in the insert of Fig. 8(a). The displacement is in *x* direction and mainly concentrated on the top of the steel tube. The vibrating mode of the second band exhibits also a displacement distribution mainly concentrated on the top of the steel tube but in *y* direction. It is worth noting that these two bands exist in all directions shown in the Note D of SI. The surface waves considered in this work are Rayleigh waves, whose displacement components on the surface only exist in the *x* and *z* directions [40]. The Rayleigh waves can excite the ITSM to vibrate in the frequency range of the first band, but not the second band, i.e., they can propagate in the ITSM in the frequency range of the first band, but not the second band [36, 44]. Therefore, the bandgap starts from the highest point of the first band. The bandgap of the ITSM for Rayleigh waves is in the range of 34-130 Hz, which is marked by the light gray part in Fig. 8(a).

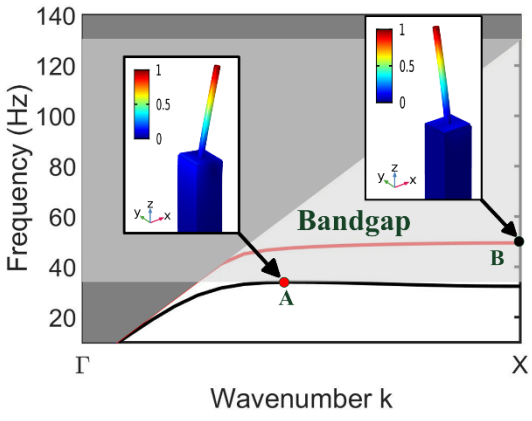

(a)

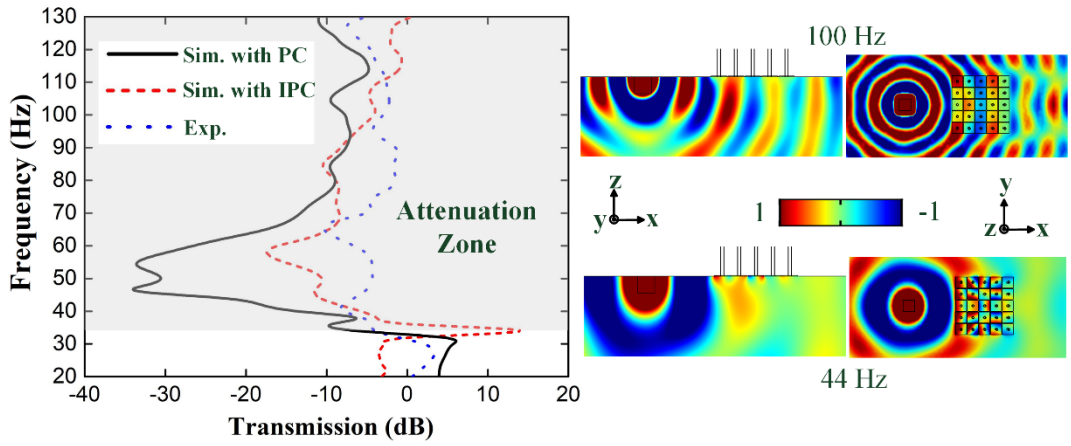

(b)

Figure 8: (a) the band structure in the ΓX direction of the first irreducible Brillouin zone of the 2D ITSM. (b) The transmission spectrum of the simulated and experimental results along ΓX direction through the 2D ITSM. The bandgap for Rayleigh waves and attenuation zone are all marked by the light gray part. The simulated results with the perfect continuity (PC) and the imperfect continuity (IPC) between substrate and man-made structures are given. The simulated results with PC of transmission of Rayleigh waves in the ITSM at 44 and 100 Hz are shown in the right side, respectively.

In Fig. 8(b), the black line is the simulation results when there is perfect continuity (PC) between the man-made structures and substrate. The red dash line is the simulation results when there is imperfect continuity (IPC) between the man-made structures and substrate. And blue dot line experimental results. The model used in the simulation is the same as the experimental site. Moreover, the influence of the continuity between the man-made structures and the substrate on the attenuation of Rayleigh waves is analyzed. A very thin PML ($t = 0.02a$) with the scaling factor s = 0.1 is added underneath all man-made structures.[37] In the range of 34-130 Hz, Rayleigh waves are attenuated significantly. It can be found that the attenuation effect in the simulated results with the PC is generally stronger than the results of the field test. However, the simulated results with the IPC are closer to the experimental results, especially in the range from 40 to 60 Hz. This is because

the simple connection between the TSs and the soil in the field test is weaker than the perfect connection in the simulation. In addition, it is worth noting that in the bandgap, experimental and simulated results all show that the attenuation of Rayleigh waves is stronger at the band of 34-70 Hz than the one of 70-130 Hz. In the cross-sectional and top views of simulation results with PC, it is easy to find that the propagation of Rayleigh waves in the ITSM is completely different at 44 and 100 Hz, respectively. (The propagation of Rayleigh waves without the ITSM is shown in Note E of SI). This is consistent with the results in Fig. 6(c): the attenuation in the bandgap generated by the local resonance is stronger than that by inverse-dispersion characteristics when the rows of the unit cell are fewer (5 rows in this work). Regarding the application, the ITSM is proposed for a metropolis with different buildings. The ITSM with an ultra-wide bandgap can be used around the metropolis to strongly attenuate seismic surface waves to protect almost all the buildings in the metropolis. If the number of the rows of the ITSM is large, for example, the ITSM with 30 rows can theoretically attenuate the energy of seismic waves hundreds of times. Also, the ITSM can be used to protect critical infrastructures, like nuclear power station.

In order to intuitively show the novelty of the 2D ITSM, a comparison table (Table 4) is prepared based on the relative widths of the first attenuation zone of the 2D ITSM we are reporting in this work, and the existing similar designs in literature. It is easy to find that the 2D ITSM has a largest relative width of the first attenuation zone just by using one kind of man-made structure. It is worth noting that the low height of the 2D ITSM makes it more competitive.

Structures	First attenuation zone (Relative width)	Remarks
2D ITSM	34 - 130 Hz (1.17)	Height less than 1 m
Trees in forest [34]	32 - 40 Hz (0.22)	Trees with an average height of 14 m

Resonant metawedge [33]	33 - 100 Hz (1.01)	Resonators with different heights
I-shaped pillar [35]	6.2 - 8.2 Hz (0.28)	
H-fractal pillar [36]	0.4 - 0.6 Hz (0.4)	
Matryoshka-like pillar [37]	5.3 - 13.1 Hz (0.85)	Pillars with height of 12.5 m
Oscillators metawedge [45]	$0.9\,f_{r1} - 3.0\,f_{r1}$ (1.08)	Oscillators with different natural frequencies

Table 4: The comparison of the ITSM with the existing similar designs in literatures

4. Conclusion

In this research, an 1D ITSM with an ultra-wide FBG has been proposed by improving the pillar-like SM. With the total mass of the pillar unchanged, the relative bandwidth of the FBG of the ITSM is about 1 at maximum. This result is much better than that of the PSM. The effects of the geometrical and material parameters of the ITSM on the FBG have been also discussed. It is found that the appearance of the plate obviously increases the center frequency and relative bandwidth of the FBG of the ITSM. The complex band structure of the ITSM has been calculated to analyze the attenuation mechanism of surface waves. It can be found that the FBG of the ITSM is composed of two parts: part 1 with surface evanescent waves and part 2 with no surface mode. We also found that this result is consistent with the PSM. The propagation of seismic surface waves in the ITSM has been also investigated. It was found that the propagation modes of surface waves in the ITSM are completely different in different parts of the FBG. In the frequency range of part 1, the seismic surface waves are significantly attenuated and almost unable to propagate to the third unit cell in the ITSM. In the frequency range of part 2, the surface waves are converted into bulk waves. Finally, we have proposed a kind of the 2D ITSM with 25 unit cells in large-scale field experiments, which can attenuate Rayleigh waves in a ultra-wide frequency range. Moreover, the lattice constant in this work is much smaller than the wavelength of the surface waves in the ultra-low frequency range. A

lower-frequency FBG can be obtained by appropriately increasing the lattice constant of the ITSM. This work not only provides new options for controlling seismic surface waves at ultra-low frequency, but also provides new design ideas for steering surface wave.

Acknowledgments

This work has been supported by la Région Grand Est, the Institut CARNOT ICEEL, and the National Natural Science Foundation of China (NNSFC) under Grant Nos. 11702017, 11991031, 11991032, 12021002 and 41974059. The first author is grateful for the support of China Scholarship Council (CSC Grant No. 202006250084).

Data availability

The data that support the findings of this study are available from the corresponding author upon reasonable request

References

[1] Y. Ding, Z. Liu, C. Qiu, J. Shi, Metamaterial with simultaneously negative bulk modulus and mass density, Physical Review Letters 99(9) (2007) 093904.
[2] X.-N. Liu, G.-K. Hu, G.-L. Huang, C.-T. Sun, An elastic metamaterial with simultaneously negative mass density and bulk modulus, Applied Physics Letters 98(25) (2011) 251907.
[3] P.A. Deymier, Acoustic metamaterials and phononic crystals, Springer Science & Business Media2013.
[4] L. Cao, Z. Yang, Y. Xu, S.-W. Fan, Y. Zhu, Z. Chen, Y. Li, B. Assouar, Flexural wave absorption by lossy gradient elastic metasurface, Journal of the Mechanics and Physics of Solids (2020) 104052.
[5] A.L. Wickeler, H.E. Naguib, Novel origami-inspired metamaterials: Design, mechanical testing and finite element modelling, Materials & Design 186 (2020) 108242.
[6] H.T. Kollmann, D.W. Abueidda, S. Koric, E. Guleryuz, N.A. Sobh, Deep learning for topology optimization of 2D metamaterials, Materials & Design 196 (2020) 109098.
[7] F. Meseguer, M. Holgado, D. Caballero, N. Benaches, J. Sánchez-Dehesa, C. López, J. Llinares, Rayleigh-wave attenuation by a semi-infinite two-dimensional elastic-band-gap crystal, Physical Review B 59(19) (1999) 12169.
[8] T.-T. Wu, L.-C. Wu, Z.-G. Huang, Frequency band-gap measurement of two-dimensional air/silicon phononic crystals using layered slanted finger interdigital transducers, Journal of Applied Physics 97(9) (2005) 094916.
[9] V. Laude, M. Wilm, S. Benchabane, A. Khelif, Full band gap for surface acoustic waves in a piezoelectric phononic crystal, Physical Review E 71(3) (2005) 036607.

[10] C. Gao, D. Halim, X. Yi, Study of bandgap property of a bilayer membrane-type metamaterial applied on a thin plate, International Journal of Mechanical Sciences 184 (2020) 105708.
[11] X. Yin, S. Zhang, G.-K. Xu, L.-Y. Zhang, Z.-Y. Gao, Bandgap characteristics of a tensegrity metamaterial chain with defects, Extreme Mechanics Letters 36 (2020) 100668.
[12] S.-H. Kim, M.P. Das, Artificial seismic shadow zone by acoustic metamaterials, Modern Physics Letters B 27(20) (2013) 1350140.
[13] G. Finocchio, O. Casablanca, G. Ricciardi, U. Alibrandi, F. Garescì, M. Chiappini, B. Azzerboni, Seismic metamaterials based on isochronous mechanical oscillators, Applied Physics Letters 104(19) (2014) 191903.
[14] S. Brûlé, E. Javelaud, S. Enoch, S. Guenneau, Experiments on seismic metamaterials: Molding surface waves, Physical Review Letters 112(13) (2014) 133901.
[15] N. Aravantinos-Zafiris, M. Sigalas, Large scale phononic metamaterials for seismic isolation, Journal of Applied Physics 118(6) (2015) 064901.
[16] Y.-F. Wang, Y.-Z. Wang, B. Wu, W. Chen, Y.-S. Wang, Tunable and Active Phononic Crystals and Metamaterials, Applied Mechanics Reviews 72(4) (2020) 040801.
[17] FEMA, Designing for Earthquakes, (2006).
[18] M. Miniaci, A. Krushynska, F. Bosia, N.M. Pugno, Large scale mechanical metamaterials as seismic shields, New Journal of Physics 18(8) (2016) 083041.
[19] X. Pu, Z. Shi, A novel method for identifying surface waves in periodic structures, Soil Dynamics and Earthquake Engineering 98 (2017) 67-71.
[20] X. Pu, Z. Shi, Surface-wave attenuation by periodic pile barriers in layered soils, Construction and Building Materials 180 (2018) 177-187.
[21] Z. Liu, X. Zhang, Y. Mao, Y. Zhu, Z. Yang, C. Chan, P. Sheng, Locally resonant sonic materials, Science 289(5485) (2000) 1734-1736.
[22] P. Sheng, X.X. Zhang, Z. Liu, C.T. Chan, Locally resonant sonic materials, Physica B: Condensed Matter 338(1-4) (2003) 201-205.
[23] D. Bigoni, S. Guenneau, A.B. Movchan, M. Brun, Elastic metamaterials with inertial locally resonant structures: Application to lensing and localization, Physical Review B 87(17) (2013) 174303.
[24] Y. Achaoui, A. Khelif, S. Benchabane, L. Robert, V. Laude, Experimental observation of locally-resonant and Bragg band gaps for surface guided waves in a phononic crystal of pillars, Physical Review B 83(10) (2011) 104201.
[25] A. Colombi, R.V. Craster, D. Colquitt, Y. Achaoui, S. Guenneau, P. Roux, M. Rupin, Elastic wave control beyond band-gaps: shaping the flow of waves in plates and half-spaces with subwavelength resonant rods, Frontiers in Mechanical Engineering 3 (2017) 10.
[26] Y. Zeng, P. Peng, Q.-J. Du, Y.-S. Wang, B. Assouar, Subwavelength seismic metamaterial with an ultra-low frequency bandgap, Journal of Applied Physics 128(1) (2020) 014901.
[27] D. Colquitt, A. Colombi, R. Craster, P. Roux, S. Guenneau, Seismic metasurfaces: Sub-wavelength resonators and Rayleigh wave interaction, Journal of the Mechanics and Physics of Solids 99 (2017) 379-393.
[28] S. Krödel, N. Thomé, C. Daraio, Wide band-gap seismic metastructures, Extreme Mechanics Letters 4 (2015) 111-117.
[29] Y. Achaoui, B. Ungureanu, S. Enoch, S. Brûlé, S. Guenneau, Seismic waves damping with arrays of inertial resonators, Extreme Mechanics Letters 8 (2016) 30-37.
[30] Y. Zeng, Y. Xu, K. Deng, P. Peng, H. Yang, M. Muzamil, Q. Du, A broadband seismic

metamaterial plate with simple structure and easy realization, Journal of Applied Physics 125(22) (2019) 224901.
[31] F. Xu, Z. Yang, X. He, L. Zhen, An underground barrier of locally resonant metamaterial to attenuate surface elastic waves in solids, AIP Advances 10(7) (2020) 075121.
[32] B. Graczykowski, F. Alzina, J. Gomis-Bresco, C. Sotomayor Torres, Finite element analysis of true and pseudo surface acoustic waves in one-dimensional phononic crystals, Journal of Applied Physics 119(2) (2016) 025308.
[33] A. Colombi, D. Colquitt, P. Roux, S. Guenneau, R.V. Craster, A seismic metamaterial: The resonant metawedge, Scientific Reports 6 (2016) 27717.
[34] A. Colombi, P. Roux, S. Guenneau, P. Gueguen, R.V. Craster, Forests as a natural seismic metamaterial: Rayleigh wave bandgaps induced by local resonances, Scientific Reports 6 (2016) 19238.
[35] Y. Zeng, Y. Xu, K. Deng, Z. Zeng, H. Yang, M. Muzamil, Q. Du, Low-frequency broadband seismic metamaterial using I-shaped pillars in a half-space, Journal of Applied Physics 123(21) (2018) 214901.
[36] Q. Du, Y. Zeng, Y. Xu, H. Yang, Z. Zeng, H-fractal seismic metamaterial with broadband low-frequency bandgaps, Journal of Physics D: Applied Physics 51(10) (2018) 105104.
[37] Y. Zeng, Y. Xu, H. Yang, M. Muzamil, R. Xu, K. Deng, P. Peng, Q. Du, A Matryoshka-like seismic metamaterial with wide band-gap characteristics, International Journal of Solids and Structures 185-186 (2020) 334-341.
[38] Y.-F. Wang, Y.-S. Wang, V. Laude, Wave propagation in two-dimensional viscoelastic metamaterials, Physical Review B 92(10) (2015) 104110.
[39] R. Cai, Y. Jin, T. Rabczuk, X. Zhuang, B. Djafari-Rouhani, Propagation and attenuation of Rayleigh and pseudo surface waves in viscoelastic metamaterials, Journal of Applied Physics 129(12) (2021) 124903.
[40] L. Rayleigh, On waves propagated along the plane surface of an elastic solid, Proceedings of the London Mathematical Society 1(1) (1885) 4-11.
[41] S. Brule, S. Enoch, S. Guenneau, Experimental evidence of auxetic features in seismic metamaterials: Ellipticity of seismic Rayleigh waves for subsurface architectured ground with holes, arXiv preprint arXiv:1809.05841 (2018).
[42] Y. Chen, Q. Feng, F. Scarpa, L. Zuo, X. Zhuang, Harnessing multi-layered soil to design seismic metamaterials with ultralow frequency band gaps, Materials & Design (2019) 107813.
[43] M. Badreddine Assouar, M. Oudich, Dispersion curves of surface acoustic waves in a two-dimensional phononic crystal, Applied Physics Letters 99(12) (2011) 123505.
[44] A. Khelif, Y. Achaoui, S. Benchabane, V. Laude, B. Aoubiza, Locally resonant surface acoustic wave band gaps in a two-dimensional phononic crystal of pillars on a surface, Physical Review B 81(21) (2010) 214303.
[45] X. Pu, A. Palermo, A. Marzani, Lamb's problem for a half-space coupled to a generic distribution of oscillators at the surface, arXiv preprint arXiv:2101.09997 (2021).